Two-Color-Driven Controllable Terahertz Generation in ITO Thin Film

Yongchang Lu, Xueqian Zhang,* Quan Xu, Wenhe Jia, Xi Feng, Xieyu Chen, Yangfan Gu, Yuanmu Yang, Weili Zhang,* and Jiaguang Han*

Read Online

ACCESS | Metrics & More | Article Recommendations | Supporting Information

ABSTRACT: Seeking new compact and controllable terahertz sources has garnered enormous interest across various disciplines. In our recent preliminary work, we have showcased the potential of an ultrathin indium tin oxide (ITO) film as an innovative platform for generating broadband terahertz waves. In this study, we conducted both experimental and theoretical investigations into a two-color femtosecond-laser-driven broadband terahertz generation in an ITO thin film. By adjusting the time delay and polarizations of the two driving pulses, we observed that the broadband terahertz waves exhibited nearly 100% amplitude modulation and 360° polarization angle tuning. To interpret the controllable processes, we employed a degenerated four-wave mixing (FWM) model. Our results indicated a correlation between the two-color interaction process and the second-order optical rectification process at the ITO film's surface, which either enhanced or suppressed the overall terahertz generation.

KEYWORDS: Terahertz generation, indium tin oxide film, two-color interaction, amplitude and polarization modulation, four-wave mixing
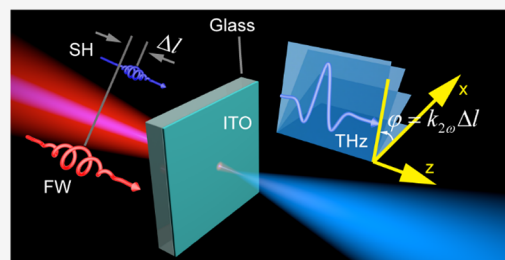
1. INTRODUCTION

The nonlinear generation of broadband terahertz (THz) fields with ultrafast lasers has attracted significant interest for both fundamental research and disruptive practical applications. Over the past three decades, various methods have been proposed, including semiconductor-based photoconductive antennas[1−3] and surface emission,[4−6] nonlinear-crystal-based optical rectification,[7,8] plasma-based wave mixing,[9−12] and so on. Research in this subject is continuously fueled to explore new materials and generation mechanisms to achieve compact, controllable, and versatile THz sources. Thin films, such as spintronic films,[13,14] layered transition metal dichalcogenides,[15,16] and graphene,[17,18] have gained lots of attention for THz generation due to their deep-subwavelength thickness, phase-matching-free nature, and novel generation mechanisms.

Indium tin oxide (ITO) films,[19,20] a widely applied transparent conducting thin-film material, have shown exceptional performance in harmonic generation,[21−24] refractive index modulation,[25−28] and all-optical light control.[29−31] In our recent work, we have demonstrated that the ITO thin films possess remarkable characteristics in broadband THz generation[32,33] when driven by one-color femtosecond laser pulses, which is attributed to the surface second-order optical rectification (SSOR) effect. The unique property of natural epsilon-near-zero (ENZ) properties exhibited by ITO films leads to a substantial enhancement of terahertz emission. However, in one single laser pumping configuration, one limitation is that THz generation in ITO thin film is mainly

achievable through oblique incidence due to the centrosymmetric surfaces of ITO. To overcome the limitations imposed from centrosymmetric surfaces, a promising alternative is the use of multicolor driving pulses based on third-order optical nonlinearity.[34] In this context, more available pump fields can interact within the ITO film even under normal incidence, where various compositions of pump field components can contribute to THz polarizations through corresponding susceptibility tensor elements. Consequently, it is expected that THz generation could be remarkably sensitive to the driving laser pulses.

In this work, we focus on investigating THz generation in ITO thin films using two-color ultrafast laser pulses. The pump laser pulses consist of a fundamental-wave (FW) pulse at 1400 nm and a second-harmonic (SH) pulse at 700 nm. By precisely tuning the pumping laser fields and controlling the time delay between the FW and SH pulses, we achieved controllable THz generation. Under colinearly polarized normal pumps, we observed nearly 100% amplitude modulation of generated THz waves. Furthermore, we discovered that under cocircularly polarized normal pumps, the generated THz waves exhibit a
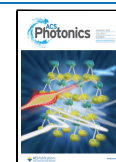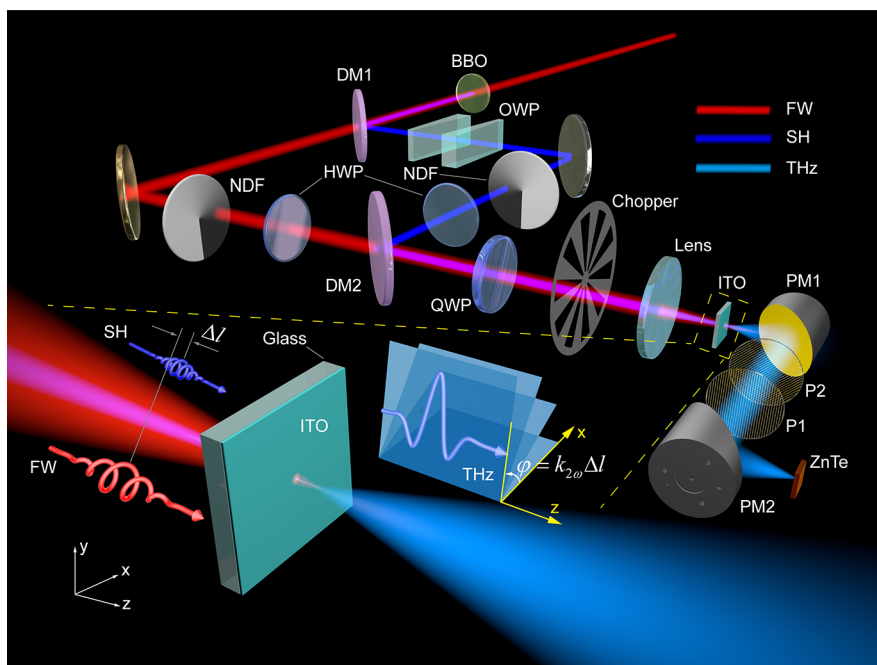
Figure 1. Schematic of the two-color interaction setup for measuring the time-resolved tunable THz generation and polarization manipulation in the ultrathin ITO film. The optical components are described as the 100 μm-thick β-barium borate (BBO) is used to generate SH beam; the dichroic mirrors (DM1, DM2) are used to separate and recombine the FW and SH beams; the neutral density filters (NDFs) and half-wave plates (HWPs) are used to control the intensity and polarization of the FW and SH beams, respectively; the quarter-wave plate is used to convert the pump beams from linearly polarized to circularly polarized; the optical wedge pairs (OWPs) are used to finely control the optical path difference between the FW and SH beams; two parabolic mirrors (PM1, PM2) are used to collimate and focus the generated THz waves, and the two THz wire-grid linear polarizers (P1, P2) are used to analyze the polarization states of the generated THz waves.
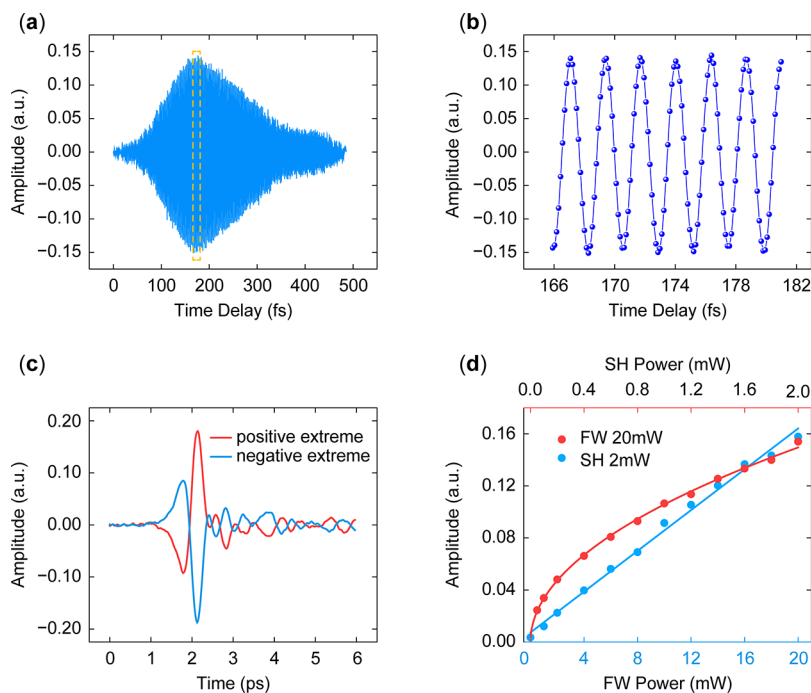

Figure 2. Time-resolved tunable THz generation via two-color interaction under normal pump. (a) Measured time-resolved phase curves of the generated THz peak amplitude versus Δt, where Δt is transformed from the relative optical path by $\Delta t = \Delta l/c$. (b) Zoomed-in view of the time-resolved phase curve in the orange dashed box in panel (a). (c) Measured THz temporal traces at the positive (red) and negative (blue) extrema in panel (b). (d) Measured power dependences of the THz peak amplitude on the FW power with a fixed SH power of 2 mW (blue dot), and on the SH power with a fixed FW power of 20 mW (red dot), respectively.

360° polarization rotation. It is worth emphasizing that the abovementioned manipulation can be achieved by operating

the time delay in a subfemtosecond resolution. To explain our experimental observations, we employed a degenerated four-

wave mixing (FWM) model, which provided a comprehensive understanding of THz generation and modulation processes. Our present work paves the way for exploring ultrafast nonlinear THz generation processes in ITO films and holds great promise for the development of compact and controllable THz sources.

2. EXPERIMENTAL SECTION

The key to the two-color interaction lies in ensuring precise temporal synchronization of the two pump pulses and their perfect overlap within the ITO material. Additionally, to fully harness the multidimensional control potential granted by the third-order nonlinear process, we needed independent control over the amplitudes, polarizations, and relative phase of the FW and SH pulses. To achieve these, we constructed a two-color THz time-domain spectroscopy system, as schematically illustrated in Figure 1. The pump laser used to drive the whole setup was from a Ti:Sapphire femtosecond laser amplifier with 800 nm central wavelength, ~35 fs pulse duration, and 1.0 kHz repetition rate. This laser was split into two parts. One was dedicated to powering an optical parameter amplifier (OPA) to generate an FW pulse at 1400 nm. The other was utilized for time-domain electro-optical sampling in a 1 mm-thick, 110-cut ZnTe crystal to detect THz pulse. To establish the two-color interaction environment required for our experiment, the FW pulse initially traversed a 100 μm-thick β-barium borate (BBO) crystal to generate the SH pulse at 700 nm. Subsequently, a dichroic mirror (DM1) was employed to separately transmit and reflect the output FW and SH pulses. Prior to their recombination using another dichroic mirror (DM2), the SH pulse passed through a quartz optical wedge pair (OWP) with a wedge angle of 1.6656° and a refractive index of n = 1.4553. By laterally adjusting their relative position using a motorized translation stage, the time delay of SH pulse can be precisely controlled with the resolution of 0.13 fs, corresponding to a phase shift of 20.22°. The power and linear polarization states of the FW and SH pulses were independently controlled by neutral density filters (NDFs) and broadband half-wave plates (HWPs) positioned along their respective paths. Finally, the FW and SH pulses were loosely focused onto the sample, i.e., a 23 nm-thick ITO film coated on a 0.7 mm-thick float glass substrate, from the backside using a lens with a 75 mm focal length. The residual pumps were filtered out using a piece of paper. The generated THz pulse was successively collimated and focused by two parabolic mirrors (PM1, PM2) onto the ZnTe crystal for field extraction. Two wire-grid linear polarizers (P1 and P2) were inserted between PM1 and PM2 for analyzing the polarization states of the generated THz pulse.

3. RESULTS AND DISCUSSION

3.1. Two-Color THz Generation and Amplitude Modulation. The two pump beams were both set x-polarized and normal incidence with approximately 20 mW of FW pulse and 2 mW of SH pulse. After carefully overlapping them at the ITO film, we unidirectionally scanned the time delay of the SH pulse using OWP. Consequently, the timely resolved THz generation was observed in the range of 486 fs, as shown in Figure 2a, where the peak amplitudes of the generated THz pulses were plotted. Figure 2b illustrates a zoomed-in view of the data in the orange dashed box in Figure 2a, exhibiting a cosine-like modulation with a period of 2.33 fs, which is

precisely aligned with the SH frequency. The modulation depth of the THz amplitude, defined as $(|A_{\max}| - |A_{\min}|)/|A_{\max}|$, approaches 100%, which can be achieved in just a 0.58 fs time delay. Figure 2c plots two particular temporal traces of the generated THz pulses corresponding to the positive and negative extrema in Figure 2b, clearly demonstrating opposite polarities. Additionally, the THz pulses at each time delay were analyzed to be linearly polarized along the x direction among the whole THz frequency spectrum. Notably, these results indicate a robust manner for the continuous amplitude modulation and binaural phase manipulation of the generated THz pulses, holding its great promise in applications of directly generating various structural THz beams. More remarkably, as the counterpart in second-order nonlinear process, integrating artificially engineered resonators with ITO film could significantly boost the interacted pump fields and thereby further unleash the potential of third-order nonlinear processes for efficient THz generation and modulation.[35]

In our measurements, we also investigated the relationships between the THz amplitude and the powers of the FW and SH pulses. Figure 2d presents two sets of experimental results displaying distinct increasing trends. For the FW power dependency, we kept the SH power constant at 2 mW while varying the FW power from 1 to 20 mW. The peak THz amplitudes, represented by blue solid circles in Figure 2d, exhibited a linear dependence on the FW power. On the other hand, when we kept the FW power fixed at 20 mW and varied the SH power from 0.05 to 2 mW, the variations in peak THz amplitudes, shown as red data points in Figure 2d, followed a square-root dependence on the SH power.

It is important to note that no THz signal was observed in the absence of the ITO film or of either the FW or SH pulses. Though there were oblique wavevector components under normal pump when using focused FW pulse, the corresponding THz generations by SSOR process will be self-canceled in our measuring configuration since the wavevector components of the focused pulse had a conical symmetry with respect to the optical axis. Even in the imperfect case of an asymmetric focusing pump or ITO film with slightly broken centrosymmetry, the SSOR contribution should not be serious in our case since the numerical aperture of the selected lens was ~0.17, which only provided small oblique wavevector components. During the measurements, we used relatively low two-color pump power, which did not exceed 22 mW. The illuminated region on the ITO sample had a radius of approximately 200 μm, corresponding to a peak optical power of 3.8 × 10^{11} W/cm². Importantly, we did not observe any optical damage or photoionization under these pump conditions. The excitation primarily involved intraband transitions within the conduction band of ITO due to the below bandgap pump photon energy, resulting in an unchanged free electron density within the ITO material.

Upon reviewing the aforementioned experimental results, we found that the oscillations of THz amplitude at the SH carrier frequency as well as the linear and square-root dependence of THz amplitude on FW and SH power, can both be effectively explained by an FWM model, which is described by a third-order nonlinear polarization equation:

$$P_{\text{THz},p}(t) \propto \chi^{(3)}_{pmnq}(2\omega, -\omega, -\omega)E_{2\omega,m}(t)E^*_{\omega,n}(t)E^*_{\omega,q}(t)$$

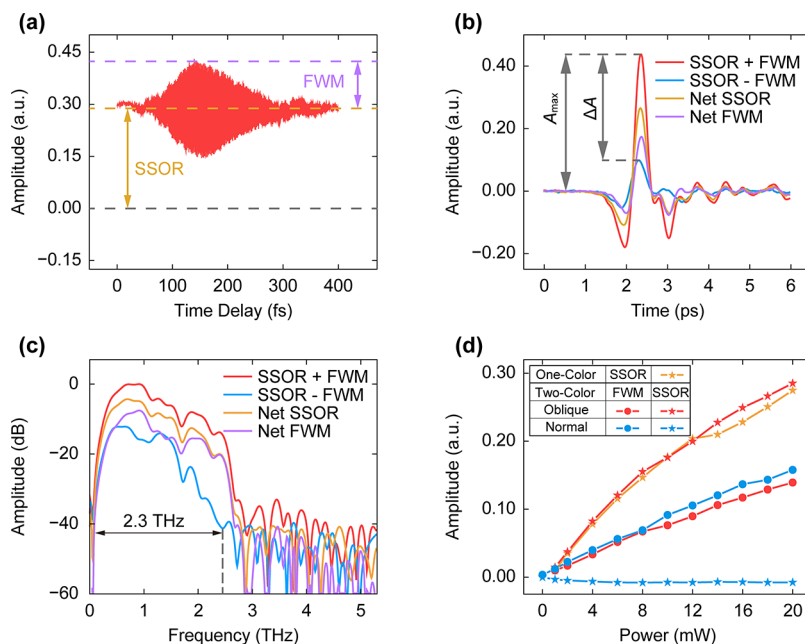$$\exp(i\Delta\varphi) + \text{c.c.} \tag{1}$$

Figure 3. Comparison of the THz generations under normal and oblique two-color pumps. (a) Measured time-resolved phase curve of the generated THz peak amplitude versus Δt under a 40° two-color pump. The vertical offset is due to the SOR contribution from the FW pump. (b) Measured THz temporal traces recorded at the maximum (red) and minimum (blue) of the phase curve envelope in panel (a). The orange one is the measured temporal trace under 40° pump of sole FW. The purple one is the extracted THz generation contributed from the sole FWM process. (c) Fourier-transformed intensity spectra of the temporal traces in panel (b). (d) Measured power dependences of the THz peak amplitudes induced by the FWM and SOR effects on the FW power under different pump conditions depicted in the inset table.

where $P_{THz,p}$ is the nonlinear polarization; $\chi^{(3)}$ is the third-order nonlinear susceptibility; $E_\omega(t)$ and $E_{2\omega}(t)$ are the temporal envelopes of FW and SH pulses with angular frequencies of ω and 2ω, respectively. The THz frequencies can be obtained either by $(2\omega - \omega - \omega)$ or by $(\omega + \omega - 2\omega)$ processes; $\Delta\varphi$ is the relative phase difference between the FW and SH pulses; the subscripts p, m, n and $q \in \{x, y, z\}$ represent the polarization states of THz, SH, and two FW pulses, respectively; *c.c.* represents the complex conjugate. In our case, $\Delta\varphi = 2\omega\Delta t$ with Δt being the time delay between the FW and SH pulses with respect to the SH pulse. In this context, the distinct power dependence can be attributed to the second- and first-order power relationships between the overall THz polarization and FW and SH electric fields, while the cosine-like curve of the THz amplitudes originated from the successively varying $\Delta\varphi$.

To give an intuitive insight of the FWM process in ITO, the coupled-wave equation is carefully calculated using measured refractive and absorption properties of the ITO film. By simply considering the ITO as a bulk material with infinite thickness and maintained material property, it is found that the amplitude of the generated THz wave reaches its maximum at a 213 nm propagation length, which is much larger than the applied film thickness here. Additionally, we measured the THz power using a Golay detector under a total pump power of 22 mW, which was ∼24 pW. This gives us a nonlinear conversion efficiency of $\eta = 1.1 \times 10^{-9}$. By substituting it into a simplified coupled-wave equation, the effective $\chi^{(3)}$ is estimated to be $\sim (6.44 + 6.85i) \times 10^{-19}$ m^{2}V^{-2}, which is comparable to previously reported values of other third-order nonlinear processes.[19] More detailed information is referred to in Supporting Information Note 1.

Driven by curiosity regarding the coexistence of one-color and two-color interactions, we further studied the THz

generation behaviors under oblique incidence. As shown in Figure 3a, the time-resolved THz peak amplitude measured under 40° *p*-polarized pumps features a vertical offset as compared with that in Figure 2a, around which the THz peak amplitudes also oscillate with the period of 2.33 fs. In this setup, the FW and SH powers remain consistent with those used in Figure 2a. The ultrafast oscillation-type modulation and the vertical offset are intuitively attributed to the FWM contribution and the SSOR contribution by the FW pulse and ITO, respectively, as no THz signal is observed under the sole SH pump. Figure 3b shows the THz temporal traces measured at the maximum (red) and minimum (blue) of the curve envelope in Figure 3a, displaying constructive enhancement (SSOR + |FWM|) and destructive suppression (SSOR − |FMW|) relationships between the SSOR and FWM contributions, respectively. Intriguingly, the addition of just 2 mW of the SH pump (1/10 of the FW power) results in a maximum amplitude modulation of the THz generation by 77.4%, defined as $\Delta A/A_{max}$ in Figure 3b. Based on these results, the THz temporal trace from the net SSOR (orange) and FWM contributions (purple) are extracted. Figure 3c illustrates the Fourier-transformed intensity spectra of these temporal traces, where the bandwidths above the noise level are all around 2.3 THz. Since FWM possesses more frequency mixing combinations, the peak THz frequency of FWM is higher than that of SSOR. The measured bandwidths are mainly limited by the phonon absorption effect of the ZnTe crystal. By applying a 0.3 mm-thick GaP crystal as a detector, the broader bandwidth is measured (see Supporting Information, Figure S3).

Figure 3d illustrates the measured power dependences of the THz peak amplitudes on the FW power under *p*-polarized normal and oblique pumping conditions. Notably, THz generation solely via SSOR under normal FW pumping (blue star) remains at the noise level since the second order
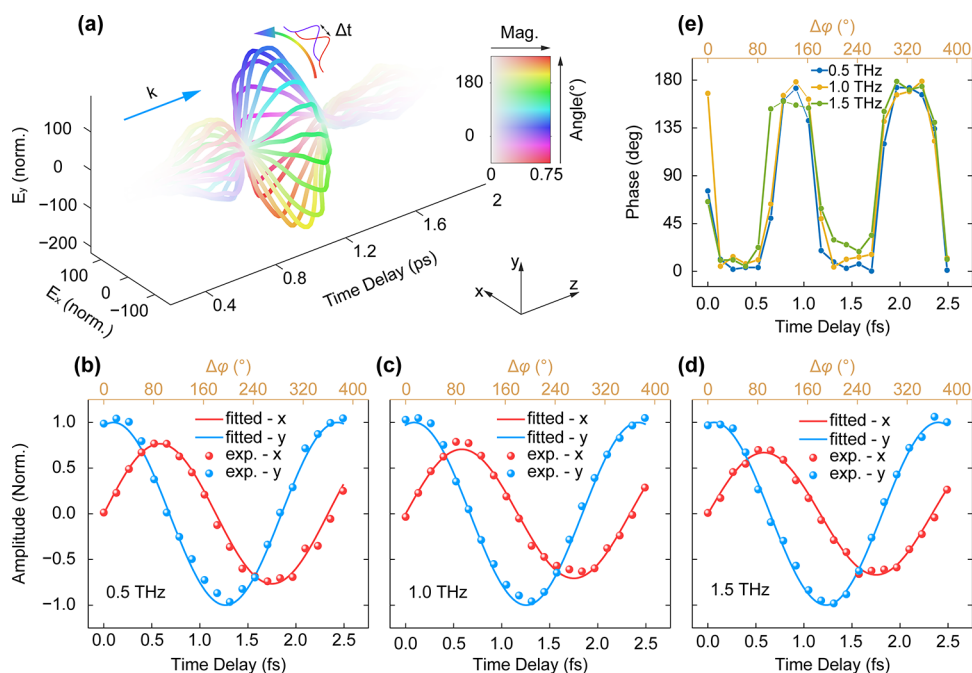
Figure 4. Time-resolved THz linear polarization control under normal LCP FW and SH pump. (a) Measured temporal traces at each time delay, where the color represents the polarization angle and the color saturation represents the magnitude of the THz electric. For clarity, higher transparency has been applied to the oscillations away from the main pulse. (b–d) Measured time-resolved amplitudes of the generated x-component (red dots) and y-component (blue dots) THz fields versus Δt at 0.5 (a), 1.0 (b), and 1.5 THz (c), respectively. The red and blue lines are the corresponding fitted results. (e) Measured phase differences between the y- and x-component THz fields versus Δt.

nonlinearity is inhibited. Furthermore, the THz generations via SSOR contribution under one-color (FW, orange star) and two-color (red star) oblique pumping conditions exhibit nearly identical amplitudes, confirming that the SH pulse does not participate in the SSOR process. In another aspect, the THz generations via FWM contribution under two-color oblique pumping conditions (red dot) are also slightly smaller than those under normal pumping conditions (blue dot). This is intriguing since the FW wavelength is around the ENZ wavelength of the ITO film, suggesting the ENZ effect should enhance the normal FW field component in ITO under oblique pumping, thereby expecting an enhancement in THz generation.

To interpret this behavior, a detailed theoretical model involving numerical simulation, FWM equations, field integration, and multiple-beam interference is carried out, where the refractive and absorption properties of the ITO film are considered as unchanged upon femtosecond laser pump. The results show that the THz generation by FWM under a 40° p-polarized oblique pump can only bring a 19% enhancement compared to that under normal incidence. This enhancement is not that obvious and can be primarily attributed to two factors: One is the loss of the ITO film in the ENZ region, which makes the normal component of the FW field acquire only a small enhancement (∼1.3 times to the tangential component at 1400 nm). The other is the tensor nature of the third-order susceptibility, which results in the generation of both tangential and normal THz field components inside the ITO film with a phase difference. However, only the field component that matches the free-space propagation mode can radiate toward the far field. Therefore, the energy of the generated THz fields cannot be fully detected. More detailed information can be found in Supporting Information Note 2. To speculate on the possible

reason for the measured results here, another effect might be introduced, i.e., the hot-electron effect, since the applied pumps were femtosecond laser pulses with large peak intensities. This would induce a red shift of the ITO plasma frequency due to the increased effective mass of the hot electrons, which pushed the ENZ wavelength away from the driven wavelength. This can lead to a further reduction of the field enhancement, which may cause a suppression of THz generation when taking the changed material property of the ITO film into account, just like the experimental observation here. This can be indicated by the measured results at higher pump power, where the suppression of THz generation under oblique pump becomes more pronounced in Figure 3d.

3.2. THz Polarization Manipulation. Two-color interaction is not only demonstrated to flexibly tune the THz amplitude but also holds the potential for controlling the THz polarization through designing the pump polarizations and tuning it with Δt, as suggested by eq 1. Since the ITO film utilized in this study is amorphous and can be treated as a homogeneous and isotropic medium, the third-order nonlinear susceptibility $\chi^{(3)}_{pmnq}$ in eq 1 is actually a fourth-order tensor with 21 nonzero elements. Under normal pumping conditions, it is simplified to eight effective elements:

$$\chi^{(3)}_{xxxx} = \chi^{(3)}_{yyyy} = \chi_1, \qquad \chi^{(3)}_{xxyy} = \chi^{(3)}_{yyxx} = \chi_2,$$
$$\chi^{(3)}_{xyxy} = \chi^{(3)}_{yxyx} = \chi_3, \qquad \chi^{(3)}_{xyyx} = \chi^{(3)}_{yxxy} = \chi_4 \qquad (2)$$

where $\chi_1 = \chi_2 + \chi_3 + \chi_4$. In our case, the measured results show $\chi_2 \approx 0$ (see Supporting Information, Figure S6). Nevertheless, the other elements still provide additional degrees of freedom for manipulating the THz polarization. Here, we consider a particular scenario of circularly polarized (CP) FW and SH pumps:

$$\mathbf{E}_\omega(t) = \frac{A}{\sqrt{2}} E_\omega(t) \exp(i\omega t) \cdot (\hat{\mathbf{x}} + \sigma_\omega i \cdot \hat{\mathbf{y}}) + \text{c.c.}$$

$$\mathbf{E}_{2\omega}(t) = \frac{B}{\sqrt{2}} E_{2\omega}(t) \exp[i(2\omega t + \Delta\varphi)] \cdot (\hat{\mathbf{x}} + \sigma_{2\omega} i \cdot \hat{\mathbf{y}}) + \text{c.c.}$$

$$(3)$$

where $\mathbf{E}_\omega$ and $\mathbf{E}_{2\omega}$ are the complex amplitudes of CP FW and SH fields with A and B being their amplitudes, $\sigma_\omega = \pm 1$ and $\sigma_{2\omega} = \pm 1$ represent their CP handedness with +1 and −1 denoting right-handed CP (RCP) and left-handed CP (LCP), respectively, and $\hat{\mathbf{x}}$ and $\hat{\mathbf{y}}$ are unit vectors. The THz polarization can then be calculated by substituting the above equations into eq 1:

$$P_{\text{THz}}(t) = \frac{A^2 B}{2\sqrt{2}} \varepsilon_0 \chi_1 E_{2\omega}(t) E_\omega^{*2}(t)(1 + \sigma_\omega \sigma_{2\omega}) \exp(i\Delta\varphi) \cdot \hat{\mathbf{x}}$$

$$+ \frac{A^2 B}{2\sqrt{2}} \varepsilon_0 \chi_1 E_{2\omega}(t) E_\omega^{*2}(t)[-i(\sigma_\omega + \sigma_{2\omega})]$$

$$\exp(i\Delta\varphi) \cdot \hat{\mathbf{y}} + \text{c.c.} \qquad (4)$$

Equation 4 reveals that when $\sigma_\omega = \sigma_{2\omega}$, the THz polarizations along the x and y directions oscillate with equal amplitudes as $\Delta\varphi$ changes. On the other hand, when $\sigma_\omega = -\sigma_{2\omega}$, the THz polarization will vanish. It should be noticed that the additional imaginary symbol i in the y component signifies that the y-polarized THz component oscillates ahead ($\sigma_\omega = \sigma_{2\omega} = -1$) or lags behind ($\sigma_\omega = \sigma_{2\omega} = 1$) the x-polarized component by 90°. Namely, the generated THz field is linearly polarized, and its orientation angle can be arbitrarily and ultrafinely controlled by changing $\Delta\varphi$ (i.e., Δt) while overall amplitude remains constant.

To verify the above derivation, THz generation under circularly polarized FW and SH pumps was experimentally investigated. In experiments, a broadband quarter-wave plate (QWP) was inserted into the combined beam after DM2, as illustrated in Figure 1. The FW and SH pulses were initially set as RCP ($\sigma_\omega = \sigma_{2\omega} = 1$) by adjusting the HWPs and QWPs. In this case, Equation 4 can be simplified to

$$P_{\text{THz}} = \frac{A^2 B}{\sqrt{2}} \varepsilon_0 \chi_1 E_{2\omega}(t) E_\omega^{*2}(t)[\cos(\Delta\varphi) \cdot \hat{\mathbf{x}} + \sin(\Delta\varphi) \cdot \hat{\mathbf{y}}]$$

$$(5)$$

which represents a counterclockwise rotation of the THz polarization. Here, the full polarization information on the generated THz waves at different Δt was resolved by extracting two orthogonally and linearly polarized components of them using P1 and P2. This was achieved by fixing the transmission axis of P1 along the z direction while altering that of P2 to either +45° or −45° (see Figure 1). In each measurement, 20 temporal traces of THz signals were recorded and averaged. Figure 4a visually exhibits the measured synthetic time-domain THz electric field traces at different Δt values, where the color indicates the polarization angle, the color saturation represents the field magnitude, and the blue arrow denotes the direction of the THz wave vector. The THz field maintains a linearly polarized feature and rotates 360° along the z direction within a variation period of 2.33 fs. The presented rotation direction of the THz polarization in Figure 4a is clockwise since the THz polarization is analyzed after PM1, where the reflection reverses the rotation direction. Namely, the actual rotation direction after the ITO film is counterclockwise, which is in agreement with eq 5.

Through coordinate transformation and Fourier transformation, the polarization states of the generated THz waves were also analyzed in the frequency domain. Figure 4b shows the measured time-resolved amplitudes of the x-component (red dots) and y-component (blue dots) THz fields at 0.5 THz as a function of Δt. The results are fitted separately using $E_x = A_x\cos(\Delta\varphi + \varphi_{0,x})$ (red line) and $E_y = A_y\sin(\Delta\varphi + \varphi_{0,y})$ (blue line) according to eq 5, where $\Delta\varphi_{0,x}$ and $\Delta\varphi_{0,y}$ are the initial phases. The fitted amplitude ratio and initial phase difference, denoted as $r_{0.5\ \text{THz}} = A_x/A_y = 0.77$ and $\Delta\varphi_{0.5\ \text{THz}} = \varphi_{0,y} - \varphi_{0,x} = 164.5°$, exhibit a small deviation from the theoretical values of $A_{0.5\ \text{THz}} = 1$ and $\Delta\varphi_{0.5\ \text{THz}} = 180°$. The amplitude deviation may be caused by the imperfect RCP states of the FW and SH pulses, while the phase deviation may be caused by the slight discrepancy in the scanning origins of $\Delta\varphi$ at different P2 orientations. Figure 4c,d shows the corresponding measured results at 1.0 and 1.5 THz, revealing similar behaviors. Here, the frequency-dependent phase delays at three frequencies have been ignored. Figure 4e shows that the phase differences between the x- and y-component THz fields at the abovementioned three frequencies almost switch between 0 and π, further indicating the generated broadband THz waves are well linearly polarized. Furthermore, we conducted experiments involving three other circularly polarized combinations of FW and SH pulses (Supporting Information and Figure S7). The results show that the maximum amplitudes of the generated THz waves when FW and SH pulses are cocircularly polarized are much larger than those observed when FW and SH are cross-circularly polarized. The unexpected nonzero THz generation under cross-circularly polarized FW and SH pumps can be attributed to the imperfect circular polarization states of pulses and the inhomogeneity of the ITO film.

In addition to the individual THz amplitude and polarization manipulations, synchronized control of them can also be achieved by simply selecting the specific FW and SH polarization combination. Our calculations indicated that in the case of elliptically polarized FW and SH pumps the generated THz fields remained linearly polarized. The overall amplitude and polarization angle of THz fields varies with Δt, and the field trajectory forms an ellipse. The shape and rotation direction of this ellipse were determined by the phase differences (θ and γ) between the x- and y-polarized components of FW and SH pulses, respectively (see Supporting Information Note 3).

4. CONCLUSIONS

We have successfully demonstrated an advanced method for all-optical time-resolved amplitude and polarization control in broadband THz generation using an ITO thin film. Our experiments utilized a 23 nm-thick ITO film and employed a two-color interaction process, which can be effectively explained using a degenerate FWM model. Our results have shown remarkable achievements in controllable THz generation. Under normal pumps, we achieved an impressive modulation of nearly 100% in THz amplitude thanks to the sole contribution of the FWM process. In addition, we successfully demonstrated a full angle polarization rotation of the generated THz pulse. By irradiating the ITO film with cocircularly polarized FW and SH pumps, we were able to achieve a complete 360° rotation of the THz polarization. Importantly, these modulations were achieved within a subfemtosecond time delay between the FW and SH pulses.

Under oblique pumps, both SSOR and FWM processes contribute to THz generation in a simple interference manner. However, the measured results here show that the ENZ effect does not give an enhanced THz generation by FWM, which may result from the finite field enhancement related to the loss and hot-electron-induced redshift of plasma frequency in the ITO film. Our findings, rooted in the intricacies of the two-color interaction process, hold great promise for a wide range of applications requiring ultrafast terahertz amplitude and polarization modulations, for example, THz communication and sensing, where even a femtosecond adjustment in the time delay can induce substantial modulation capabilities.

■ ASSOCIATED CONTENT

ⓈⒾ Supporting Information

The Supporting Information is available free of charge at https://pubs.acs.org/doi/10.1021/acsphotonics.3c01495.

> (1) General derivation of the FWM process for THz generation in ITO; (2) measured normalized spectra of the FWM-based THz waves detected by a 1 mm-thick ZnTe crystal and a 0.3 mm-thick GaP crystal; (3) THz generation through FWM process in the ITO film; (4) measured *x*-components of the generated THz waves under colinearly polarized and cross-linearly polarized two-color pump; (5) measured time-resolved peak amplitudes of the generated *x*-component THz fields under four circularly polarized pump combinations of the FW and SH pulses; (6) synchronized control of amplitude and polarization of the generated THz waves (PDF)

■ AUTHOR INFORMATION

Corresponding Authors

Xueqian Zhang − *Center for Terahertz waves and College of Precision Instrument and Optoelectronics Engineering, Tianjin University and the Key Laboratory of Optoelectronics Information and Technology (Ministry of Education), Tianjin 300072, China;* Ⓞorcid.org/0000-0001-7712-3365; Email: alearn1988@tju.edu.cn

Weili Zhang − *School of Electrical and Computer Engineering, Oklahoma State University, Stillwater, Oklahoma 74078, United States;* Email: weili.zhang@okstate.edu

Jiaguang Han − *Center for Terahertz waves and College of Precision Instrument and Optoelectronics Engineering, Tianjin University and the Key Laboratory of Optoelectronics Information and Technology (Ministry of Education), Tianjin 300072, China; Guangxi Key Laboratory of Optoelectronic Information Processing, School of Optoelectronic Engineering, Guilin University of Electronic Technology, Guilin 541004, P. R. China;* Ⓞorcid.org/0000-0001-9425-9635; Email: jiaghan@tju.edu.cn

Authors

Yongchang Lu − *Center for Terahertz waves and College of Precision Instrument and Optoelectronics Engineering, Tianjin University and the Key Laboratory of Optoelectronics Information and Technology (Ministry of Education), Tianjin 300072, China*

Quan Xu − *Center for Terahertz waves and College of Precision Instrument and Optoelectronics Engineering, Tianjin University and the Key Laboratory of Optoelectronics Information and Technology (Ministry of Education),*

Tianjin 300072, China; Ⓞorcid.org/0000-0001-9246-3253

Wenhe Jia − *State Key Laboratory of Precision Measurement Technology and Instruments, Department of Precision Instrument, Tsinghua University, Beijing 100084, China*

Xi Feng − *Center for Terahertz waves and College of Precision Instrument and Optoelectronics Engineering, Tianjin University and the Key Laboratory of Optoelectronics Information and Technology (Ministry of Education), Tianjin 300072, China*

Xieyu Chen − *Center for Terahertz waves and College of Precision Instrument and Optoelectronics Engineering, Tianjin University and the Key Laboratory of Optoelectronics Information and Technology (Ministry of Education), Tianjin 300072, China; Research Center for Intelligent Chips and Devices, Zhejiang Lab, Hangzhou 311121, China;* Ⓞorcid.org/0000-0003-1574-3782

Yangfan Gu − *Center for Terahertz waves and College of Precision Instrument and Optoelectronics Engineering, Tianjin University and the Key Laboratory of Optoelectronics Information and Technology (Ministry of Education), Tianjin 300072, China*

Yuanmu Yang − *State Key Laboratory of Precision Measurement Technology and Instruments, Department of Precision Instrument, Tsinghua University, Beijing 100084, China;* Ⓞorcid.org/0000-0002-5264-0822

Complete contact information is available at:
https://pubs.acs.org/10.1021/acsphotonics.3c01495

Author Contributions

J.H., X.Z., and Y.L. conceived the idea; Y.L. performed the measurements and analyzed the data; Y.L. and X.Z. derived the theory; X.Z. J.H., and W.Z supervised the project; all the authors discussed the results and reviewed the manuscript.

Notes

The authors declare no competing financial interest.

■ REFERENCES

(1) Auston, D. H.; Cheung, K. P.; Smith, P. R. Picosecond photoconducting Hertzian dipoles. *Appl. Phys. Lett.* **1984**, *45*, 284−286.

(2) Roehle, H.; Dietz, R. J. B.; Hensel, H. J.; Böttcher, J.; Künzel, H.; Stanze, D.; Schell, M.; Sartorius, B. Next generation 1.5 μm terahertz antennas: mesa-structuring of InGaAs/InAlAs photoconductive layers. *Opt. Express* **2010**, *18*, 2296−2301.

(3) Berry, C. W.; Wang, N.; Hashemi, M. R.; Unlu, M.; Jarrahi, M. Significant performance enhancement in photoconductive terahertz optoelectronics by incorporating plasmonic contact electrodes. *Nat. Commun.* **2013**, *4*, 1622.

(4) Zhang, X. C.; Hu, B. B.; Darrow, J. T.; Auston, D. H. Generation of femtosecond electromagnetic pulses from semiconductor surfaces. *Appl. Phys. Lett.* **1990**, *56*, 1011−1013.

(5) Heyman, J. N.; Coates, N.; Reinhardt, A.; Strasser, G. Diffusion and drift in terahertz emission at GaAs surfaces. *Appl. Phys. Lett.* **2003**, *83*, 5476−5478.

(6) Fan, Z.; Xu, M.; Huang, Y.; Lei, Z.; Zheng, L.; Zhang, Z.; Zhao, W.; Zhou, Y.; Wang, X.; Xu, X.; Liu, Z. Terahertz Surface Emission from MoSe2 at the Monolayer Limit. *ACS Appl. Mater. Interfaces* **2020**, *12*, 48161−48169.

(7) Stepanov, A. G.; Kuhl, J.; Kozma, I. Z.; Riedle, E.; Almási, G.; Hebling, J. Scaling up the energy of THz pulses created by optical rectification. *Opt. Express* **2005**, *13*, 5762−5768.

(8) Vicario, C.; Monoszlai, B.; Hauri, C. P. Gv/m Single-Cycle Terahertz Fields from a Laser-Driven Large-Size Partitioned Organic Crystal. *Phys. Rev. Lett.* **2014**, *112*, No. 213901.

(9) Xie, X.; Dai, J. M.; Zhang, X. C. Coherent control of THz wave generation in ambient air. *Phys. Rev. Lett.* **2006**, *96*, No. 075005.

(10) Zhang, Z. L.; Chen, Y. P.; Chen, M.; Zhang, Z.; Yu, J.; Sheng, Z. M.; Zhang, J. Controllable Terahertz Radiation from a Linear-Dipole Array Formed by a Two-Color Laser Filament in Air. *Phys. Rev. Lett.* **2016**, *117*, No. 243901.

(11) Dey, I.; Jana, K.; Fedorov, V. Y.; Koulouklidis, A. D.; Mondal, A.; Shaikh, M.; Sarkar, D.; Lad, A. D.; Tzortzakis, S.; Couairon, A.; Kumar, G. R. Highly efficient broadband terahertz generation from ultrashort laser filamentation in liquids. *Nat. Commun.* **2017**, *8*, 1184.

(12) Koulouklidis, A. D.; Gollner, C.; Shumakova, V.; Fedorov, V. Y.; Pugzlys, A.; Baltuska, A.; Tzortzakis, S. Observation of extremely efficient terahertz generation from mid-infrared two-color laser filaments. *Nat. Commun.* **2020**, *11*, 292.

(13) Seifert, T.; Jaiswal, S.; Martens, U.; Hannegan, J.; Braun, L.; Maldonado, P.; Freimuth, F.; Kronenberg, A.; Henrizi, J.; Radu, I.; Beaurepaire, E.; Mokrousov, Y.; Oppeneer, P. M.; Jourdan, M.; Jakob, G.; Turchinovich, D.; Hayden, L. M.; Wolf, M.; Munzenberg, M.; Klaui, M.; Kampfrath, T. Efficient metallic spintronic emitters of ultrabroadband terahertz radiation. *Nat. Photonics* **2016**, *10*, 483−488.

(14) Qiu, H. S.; Zhou, L. F.; Zhang, C. H.; Wu, J. B.; Tian, Y. Z.; Cheng, S. D.; Mi, S. B.; Zhao, H. B.; Zhang, Q.; Wu, D.; Jin, B. B.; Chen, J.; Wu, P. H. Ultrafast spin current generated from an antiferromagnet. *Nat. Phys.* **2021**, *17*, 388−394.

(15) Huang, Y.; Zhu, L.; Zhao, Q.; Guo, Y.; Ren, Z.; Bai, J.; Xu, X. Surface Optical Rectification from Layered MoS2 Crystal by THz Time-Domain Surface Emission Spectroscopy. *ACS Appl. Mater. Interfaces* **2017**, *9*, 4956−4965.

(16) Zhang, L.; Huang, Y.; Zhu, L.; Yao, Z.; Zhao, Q.; Du, W.; He, Y.; Xu, X. Polarized THz Emission from In-Plane Dipoles in Monolayer Tungsten Disulfide by Linear and Circular Optical Rectification. *Adv. Opt. Mater.* **2019**, *7*, 1801314.

(17) Otsuji, T.; Tombet, S. B.; Satou, A.; Ryzhii, M.; Ryzhii, V. Terahertz-wave generation using graphene: Toward new types of terahertz lasers. *Proc. IEEE* **2013**, 1−13.

(18) Maysonnave, J.; Huppert, S.; Wang, F.; Maero, S.; Berger, C.; de Heer, W.; Norris, T. B.; De Vaulchier, L. A.; Dhillon, S.; Tignon, J.; Ferreira, R.; Mangeney, J. Terahertz Generation by Dynamical Photon Drag Effect in Graphene Excited by Femtosecond Optical Pulses. *Nano Lett.* **2014**, *14*, 5797−5802.

(19) Reshef, O.; De Leon, I.; Alam, M. Z.; Boyd, R. W. Nonlinear optical effects in epsilon-near-zero media. *Nat. Rev. Phys.* **2019**, *4*, 535−551.

(20) Jaffray, W.; Saha, S.; Shalaev, V. M.; Boltasseva, A.; Ferrera, M. Transparent conducting oxides: from all-dielectric plasmonics to a new paradigm in integrated photonics. *Adv. Opt Photonics* **2022**, *14*, 148−208.

(21) Aouani, H.; Rahmani, M.; Navarro-Cía, M.; Maier, S. A. Third-harmonic-upconversion enhancement from a single semiconductor nanoparticle coupled to a plasmonic antenna. *Nat. Nanotechnol.* **2014**, *9*, 290−294.

(22) Capretti, A.; Wang, Y.; Engheta, N.; Dal Negro, L. Enhanced third-harmonic generation in Si-compatible epsilon-near-zero indium tin oxide nanolayers. *Opt. Lett.* **2015**, *40*, 1500−1503.

(23) Capretti, A.; Wang, Y.; Engheta, N.; Dal Negro, L. Comparative Study of Second-Harmonic Generation from Epsilon-Near-Zero Indium Tin Oxide and Titanium Nitride Nanolayers Excited in the Near-Infrared Spectral Range. *ACS Photonics* **2015**, *2*, 1584−1591.

(24) Tian, W.; Liang, F.; Lu, D.; Yu, H.; Zhang, H. Highly efficient ultraviolet high-harmonic generation from epsilon-near-zero indium tin oxide films. *Photonics Res.* **2021**, *9*, 317−323.

(25) Alam, M. Z.; De Leon, I.; Boyd, R. W. Large optical nonlinearity of indium tin oxide in its epsilon-near-zero region. *Science* **2016**, *352*, 795−797.

(26) Huang, Y.-W.; Lee, H. W. H.; Sokhoyan, R.; Pala, R. A.; Thyagarajan, K.; Han, S.; Tsai, D. P.; Atwater, H. A. Gate-Tunable Conducting Oxide Metasurfaces. *Nano Lett.* **2016**, *16*, 5319−5325.

(27) Alam, M. Z.; Schulz, S. A.; Upham, J.; De Leon, I.; Boyd, R. W. Large optical nonlinearity of nanoantennas coupled to an epsilon-near-zero material. *Nat. Photonics* **2018**, *12*, 79−83.

(28) Wang, H.; Dai, X.; Du, K.; Gao, K.; Zhang, W.; Chua, S. J.; Mei, T. Tuning epsilon-near-zero wavelength of indium tin oxide film via annealing. *J. Phys. D: Appl. Phys.* **2020**, *53*, 225108.

(29) Guo, P. J.; Schaller, R. D.; Ketterson, J. B.; Chang, R. P. H. Ultrafast switching of tunable infrared plasmons in indium tin oxide nanorod arrays with large absolute amplitude. *Nat. Photonics* **2016**, *10*, 267−273.

(30) Clerici, M.; Kinsey, N.; DeVault, C.; Kim, J.; Carnemolla, E. G.; Caspani, L.; Shaltout, A.; Faccio, D.; Shalaev, V.; Boltasseva, A.; Ferrera, M. Controlling hybrid nonlinearities in transparent conducting oxides via two-colour excitation. *Nat. Commun.* **2017**, *8*, 15829.

(31) Bohn, J.; Luk, T. S.; Tollerton, C.; Hutchings, S. W.; Brener, I.; Horsley, S.; Barnes, W. L.; Hendry, E. All-optical switching of an epsilon-near-zero plasmon resonance in indium tin oxide. *Nat. Commun.* **2021**, *12*, 1017.

(32) Jia, W.; Liu, M.; Lu, Y.; Feng, X.; Wang, Q.; Zhang, X.; Ni, Y.; Hu, F.; Gong, M.; Xu, X.; Huang, Y.; Zhang, W.; Yang, Y.; Han, J. Broadband terahertz wave generation from an epsilon-near-zero material. *Light: Sci. Appl.* **2021**, *10*, 11.

(33) Feng, X.; Wang, Q.; Lu, Y.; Xu, Q.; Zhang, X.; Niu, L.; Chen, X.; Li, Q.; Han, J.; Zhang, W. Direct emission of broadband terahertz cylindrical vector Bessel beam. *Appl. Phys. Lett.* **2021**, *119*, 221110.

(34) Boyd, R. W.; Gaeta, A. L.; Giese, E. Nonlinear optics. In *Springer Handbook of Atomic, Molecular, and Optical Physics*; Springer, Cham, 2020; pp 26−27 DOI: 10.1007/978-3-030-73893-8_76.

(35) Lu, Y. C.; Feng, X.; Wang, Q. W.; Zhang, X. Q.; Fang, M.; Sha, W. E. I.; Huang, Z. X.; Xu, Q.; Niu, L.; Chen, X. Y.; Ouyang, C. M.; Yang, Y. M.; Zhang, X. X.; Plum, E.; Zhang, S.; Han, J. G.; Zhang, W. L. Integrated Terahertz Generator-Manipulators Using Epsilon-near-Zero-Hybrid Nonlinear Metasurfaces. *Nano Lett.* **2021**, *21*, 7699−7707.